# Behind the logarithmic growth of inner-scaled wall-pressure variance

**By J. M. O. Massey, J. C. Klewicki† AND B. J. McKeon**

In high-Reynolds-number zero-pressure-gradient turbulent channel flow, the inner-scaled wall-pressure variance follows a logarithmic increase with frictional Reynolds number of the form $\langle p_w^{+2} \rangle = B_{\mathcal{L}} + A_{\mathcal{Q}} \ln \delta^+$. We consider the two sources of the pressure Poisson equation: a linear (i.e., rapid) term linked to mean shear and a nonlinear (i.e., slow) term from quadratic velocity fluctuations. The goal of this paper is to provide a mechanistic link between the sources of the pressure Poisson equation and the coefficients in the inner-scaled variance form above. We tie the offset $B_{\mathcal{L}}$ to the linear source and connect the coefficient $A_{\mathcal{Q}}$ to the nonlinear source. The illustrative dataset is direct numerical simulation (DNS) at $\delta^+ \approx 550$, although the principal contribution is the establishment of a mechanistic link that allows us to connect well-known high-$\delta^+$ scalings of wall-bounded turbulence. Through consideration of the spectral content of the sources and the integral solution method of the Poisson equation, we find that the linear source contribution sits in the buffer layer and maps to the near-wall cycle. This contribution remains $\delta^+$ invariant in inner scaling, thus contributing the offset $B_{\mathcal{L}}$. The interfacial region between uniform momentum zones in the log layer (fissures) concentrates strain and vorticity contributions in the log layer and contains an increasingly large proportion of the strain and vorticity. We show that fissures act as a compact carrier for the source terms, with the nonlinear term especially prominent in this region. Then, by considering the inertial layer statistics, we tie the changing nonlinear contribution to $A_{\mathcal{Q}}$.

## 1. Introduction

Wall-pressure fluctuations in turbulent wall-bounded flows underpin acoustic noise, structural fatigue, and the performance of flow-control devices. In incompressible turbulence, the pressure satisfies a Poisson equation whose right-hand side contains two source terms: a linear (rapid) term coupling the mean shear to the fluctuating velocity field and a nonlinear (slow) term from quadratic velocity–velocity interactions; a viscous (Stokes) term arises from the Neumann boundary condition enforcing no slip at the wall. As the friction Reynolds number, $\delta^+ \equiv \delta u_\tau / \nu$, increases, the viscous contribution becomes progressively less important and the linear and nonlinear mechanisms dominate (Kim 1989; Hoyas & Jiménez 2006; Gerolymos *et al.* 2013).

Experiments and simulations have mapped the spectral and spatial origins of wall pressure: High frequencies are associated with the near-wall cycle, intermediate frequencies with the logarithmic region, and low frequencies with the outer flow (Farabee & Casarella 1991; Gibeau & Ghaemi 2021; Dacome *et al.* 2025; Deshpande *et al.* 2025*a*). DNS at moderate $\delta^+$ confirms that buffer layer eddies contribute strongly to both linear and nonlinear pressure, with viscous effects confined to the smallest scales (Kim 1989; Choi & Moin 1990; Chang *et al.* 1999; Hu *et al.* 2006; Lee & Moser 2015; Anantharamu

† University of Melbourne

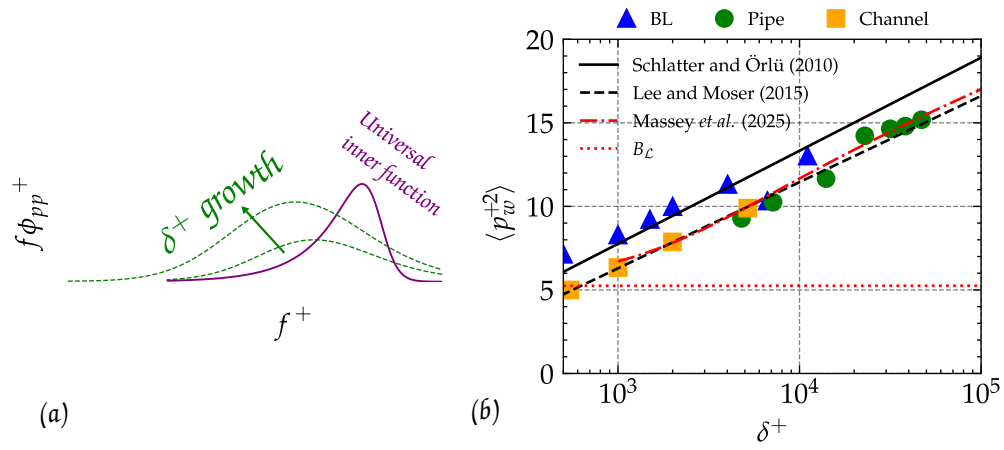


FIGURE 1. (a) Schematic of the wall-pressure spectra from Massey *et al.* (2025), showing a universal—$\delta^+$-independent—inner function and a $\delta^+$-dependent outer function responsible for modelling the contribution from outer-scaled motions. (b) $\langle p_w^{+2} \rangle$ for various DNS and experiments, showing the $\ln \delta^+$ growth. Blue triangles represent boundary layer data from Fritsch *et al.* (2020, 2022), green circles represent pipe data from Dacome *et al.* (2025), and orange squares represent channel data from Lee & Moser (2015). The red dotted line is the variance from the universal inner function, showing that it contributes an $O(1)$ offset, $B_\mathcal{L}$, when the inner function is fully developed.

& Mahesh 2020; Yang & Yang 2022). The wall-normal structure of the sources has been examined directly (Kim 1989; Anantharamu & Mahesh 2020). More broadly, wall-flow theory points to inner (viscous-scaled) and outer (boundary layer–scaled) regions (Bradshaw 1967; Panton *et al.* 2017; Deshpande *et al.* 2025*b*), and pressure can be modeled as contributions from these separate regions. Figure 1(a) summarizes the procedure proposed by Massey *et al.* (2025).

A key empirical observation, from high-$\delta^+$ boundary layers and pipes (Klewicki *et al.* 2008; Fritsch *et al.* 2020, 2022; Dacome *et al.* 2025) as well as from DNS flows (Hoyas & Jiménez 2006; Schlatter & Örlü 2010; Lee & Moser 2015; Pirozzoli & Wei 2025), is the logarithmic growth of the inner-scaled wall-pressure variance, $\langle p_w^{+2} \rangle \propto \ln \delta^+$, where $p_w^+ \equiv p_w/(\rho u_\tau^2) \equiv p_w/\tau_w$ (Figure 1(b)). Matched-asymptotic descriptions reproduce this growth (Panton *et al.* 2017), which is consistent with a progressive broadening of the low-wavenumber portion of the wall-pressure spectra. This evidence from Panton *et al.* (2017) suggests that the responsible physical processes are tied to the broadening of the log layer connecting the buffer and outer layer.

With homogeneous Neumann boundary conditions, the Green's function of the Poisson operator decays with wall-normal distance $y$ and in Fourier space, with the streamwise–spanwise wavenumber magnitude $k = \sqrt{k_x^2 + k_z^2}$. Approximately, the Green's function decays proportionally to $\mathrm{e}^{-ky}$ (Anantharamu & Mahesh 2020); short-wavelength pressure fluctuations are supplied predominantly by near-wall source terms, whereas long-wavelength pressure is supplied by sources farther from the wall. This provides a bridge between wall-pressure statistics and the wall-normal distribution of the pressure sources. This nonlocal mapping motivates a relation between polar spectral content at the wall and the locations and types of Poisson sources across $y$.

A growing body of theory, DNS, and experimental work indicates that the inertial re-

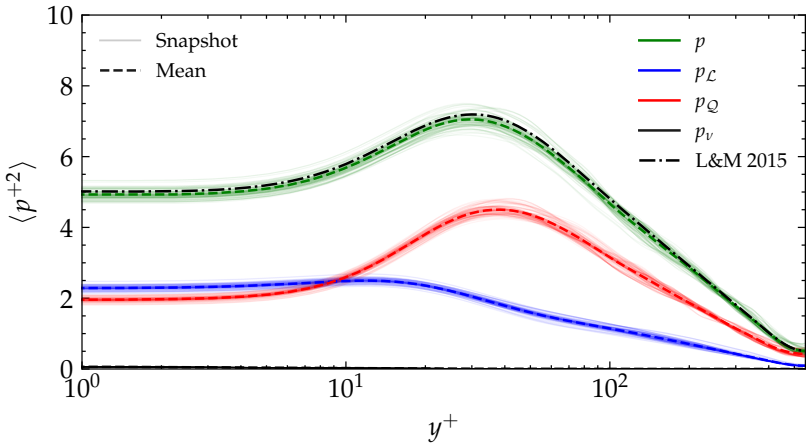


FIGURE 2. Instantaneous and mean r.m.s. profiles of the pressure across a half-channel width at $\delta^+ \approx 550$ and a comparison to the r.m.s. reported by Lee & Moser (2015).

gion organizes into large uniform-momentum zones (UMZs) separated by narrow, sheet-like fissures bearing concentrated spanwise vorticity (Meinhart & Adrian 1995; Chauhan *et al.* 2014; De Silva *et al.* 2017; Heisel *et al.* 2022) and in which enstrophy and strain are both large and strongly correlated. Fissures originate from vorticity stretching and tilting through the viscous and buffer layers, subsequently aligning in the streamwise direction under the action of mean shear (Klewicki 2013; Morrill-Winter & Klewicki 2013). In this UMZ-vortical-fissure picture, the fissure thickness, when scaled by outer length, decreases approximately as $1/\sqrt{\delta^+}$, while the streamwise velocity jump across a fissure is $O(u_\tau)$; both are central empirical inputs in minimal models that reproduce turbulent statistics at high $\delta^+$ (Bautista *et al.* 2019). Theoretical analyses of the mean momentum equation further support the view that with increasing $\delta^+$ an increasing fraction of the vorticity outside the buffer region is confined within such narrow fissures that disperse across a hierarchy of wall-normal layers (Klewicki 2013; Morrill-Winter & Klewicki 2013).

In incompressible wall turbulence at high $\delta^+$, the wall-pressure variance obeys

$$\langle p_w^{+2} \rangle = B_{\mathcal{L}} + A_{\mathcal{Q}} \ln \delta^+ \ . \tag{1.1}$$

In this paper, we link Eq. (1.1) to the processes governing the behavior of the Poisson sources themselves. Using channel DNS at $\delta^+ \approx 550$, we show that the elliptical attenuation of the Green's function maps contributions from the source at $yk \approx O(1)$. The root mean square (r.m.s.) of the source terms shows that the linear source peaks in the buffer layer, while the nonlinear source is made up of a balance of strain and enstrophy peaking in the inertial layer. Next, we show that the linear source is tied to the near-wall cycle and provides a $\delta^+$-independent $O(1)$ offset to $\langle p_w^{+2} \rangle$, arising as $B_{\mathcal{L}}$ (Eq.(1.1)). Finally, we show that inertial layer fissures act as compact carriers of the nonlinear source that contributes to $A_{\mathcal{Q}}$. This connection of the nonlinear source to inertial layer processes, and thus statistics, provides the mechanistic link between the nonlinear source and the $\ln \delta^+$ growth of $\langle p_w^{+2} \rangle$.

## 2. Components of the pressure Poisson equation

Following Mansour *et al.* (1988) and Kim (1989), and using the Einstein summation convention, we find that the fluctuating pressure satisfies

$$\partial_i\partial_i p = \underbrace{-\,2\,\frac{\mathrm{d}U}{\mathrm{d}y}\,\partial_x v}_{\text{linear }(\mathcal{L})} + \underbrace{-\,\partial_j u_k\,\partial_k u_j}_{\text{nonlinear }(\mathcal{Q})}\ , \tag{2.1}$$

where $\tilde{u_i} = U_i + u_i$. Rewritten in vorticity/strain form (Bradshaw & Koh 1981), the equation reads

$$\partial_i\partial_i p = \underbrace{2\,\Omega_z\,\partial_x v}_{\mathcal{L}} + \underbrace{\tfrac{1}{2}\,\omega_i\omega_i}_{\mathcal{T}} - \underbrace{S_{ij}S_{ij}}_{\mathcal{S}}\ , \tag{2.2}$$

where

$$S_{ij} = \tfrac{1}{2}(\partial_i u_j + \partial_j u_i), \qquad \omega_i = \varepsilon_{ijk}\,\partial_j u_k, \qquad \Omega_z = -\,\frac{\mathrm{d}U}{\mathrm{d}y}\ . \tag{2.3}$$

We define the pressure components by

$$\partial_i\partial_i p_{\mathcal{L}} = \mathcal{L}, \qquad \left(\partial_y p_{\mathcal{L}}\right)\big|_{y_w} = 0, \tag{2.4a}$$

$$\partial_i\partial_i p_{\mathcal{Q}} = \mathcal{Q} = \mathcal{T} - \mathcal{S}, \qquad \left(\partial_y p_{\mathcal{Q}}\right)\big|_{y_w} = 0, \tag{2.4b}$$

$$\partial_i\partial_i p_{\mathcal{V}} = 0, \qquad \left(\partial_y p_{\mathcal{V}}\right)\big|_{y_w} = \nu Re^{-1}\,\partial_j\partial_j v\ . \tag{2.4c}$$

It follows that

$$p = p_{\mathcal{L}} + p_{\mathcal{Q}} + p_{\mathcal{V}}\ , \tag{2.5}$$

where $p_{\mathcal{L}}$, $p_{\mathcal{Q}}$, and $p_{\mathcal{V}}$ are the linear, nonlinear, and viscous components of the pressure, respectively.

Let $\widehat{\cdot}$ denote the $(k_x, k_z)$ Fourier transform and $k = \sqrt{k_x^2 + k_z^2} > 0$. In a channel $y \in [-1, 1]$ with homogeneous Neumann boundary conditions, the solution of Eq. (2.1) for the linear and nonlinear sources $\mathcal{M} \in \{\mathcal{L}, \mathcal{Q}\}$ admits the integral representation

$$\widehat{p}_{\mathcal{M}}(k, y; \delta^+) = \int_{-1}^{1} g(k;\, y, \eta)\,\widehat{\mathcal{M}}(\eta, k; \delta^+)\,\mathrm{d}\eta\ , \tag{2.6a}$$

$$g(k;\, y, \eta) = -\frac{\cosh\big(k(1 - y_>)\big)\,\cosh\big(k(1 + y_<)\big)}{k\,\sinh(2k)}\ , \tag{2.6b}$$

with $y_< = \min(y, \eta)$ and $y_> = \max(y, \eta)$, where $\eta \in [-1, 1]$ is the integration variable. The viscous component $p_{\mathcal{V}}$ is obtained through enforcement of no slip via the Neumann boundary condition.

Evaluating Eq. (2.6) at either wall yields a convolution between the sources and a single-wall kernel. For the bottom wall ($y = -1$) and top wall ($y = +1$),

$$\widehat{p}_{\mathcal{M},w^-}(k; \delta^+) = \int_{-1}^{1} G^-(k, \eta)\,\widehat{\mathcal{M}}(\eta, k; \delta^+)\,\mathrm{d}\eta, \quad G^-(k, \eta) = -\,\frac{1}{k}\,\frac{\cosh\big(k(1 - \eta)\big)}{\sinh(2k)}, \tag{2.7a}$$

$$\widehat{p}_{\mathcal{M},w^+}(k; \delta^+) = \int_{-1}^{1} G^+(k, \eta)\,\widehat{\mathcal{M}}(\eta, k; \delta^+)\,\mathrm{d}\eta, \quad G^+(k, \eta) = -\,\frac{1}{k}\,\frac{\cosh\big(k(1 + \eta)\big)}{\sinh(2k)}. \tag{2.7b}$$

Writing the hyperbolic functions in exponential form makes the wall-normal attenuation explicit,

$$G^{-}(k,\eta) = -\frac{1}{k}\frac{\mathrm{e}^{-k(1+\eta)} + \mathrm{e}^{-k(3-\eta)}}{1-\mathrm{e}^{-4k}} \quad \xrightarrow[k\gg 1]{} \quad -\frac{1}{k}\mathrm{e}^{-k(1+\eta)}, \tag{2.8}$$

so that each Fourier mode decays exponentially with the wall-normal distance from the source to the wall. Equivalently, the full-field kernel in Eq. (2.6) has the leading-order form

$$g(k;y,\eta) \;\sim\; -\frac{1}{2k}\mathrm{e}^{-k|y-\eta|}, \tag{2.9}$$

demonstrating the expected elliptic attenuation: Contributions at wavenumber $k$ are exponentially suppressed away from their source with characteristic scale $1/k$. Below, we focus on the wall pressure and its decomposition,

$$p_w \;=\; (p_{\mathcal{L}})_w + (p_{\mathcal{Q}})_w + (p_{\mathcal{V}})_w, \tag{2.10}$$

with each component obtained by substituting $\widehat{\mathcal{M}}$ into Eq. (2.7), and we drop the $\cdot_w$ subscript for brevity.

The dataset we are using is a previously published channel-flow DNS at $\delta^+ \approx 550$ (Toedtli 2025; Huang *et al.* 2025) that employs the method of Flores & Jiménez (2006). Figure 2 shows a comparison with results from Lee & Moser (2015) and Panton *et al.* (2017) and confirms that we reproduce $\langle p^2\rangle^+$ and that the split into $\mathcal{V}$, $\mathcal{L}$, and $\mathcal{Q}$ is consistent. The nonlinear pressure variance is comparable to or larger than the linear contribution everywhere except very near the wall, with the mean-square nonlinear source peaking near $y^+ \approx 20$, in line with previous work (Kim 1989; Panton *et al.* 2017; Yang & Yang 2022).

## 3. Source-term structure

As noted by Kim (1989)and Hoyas & Jiménez (2006), $\mathcal{V}$ is subdominant and becomes negligible with increasing $\delta^+$; we therefore focus on $\mathcal{L}$ and $\mathcal{Q}$ in the following analysis.

Figure 3(a) shows that the $\mathcal{L}$ energy is concentrated near $y^+ \approx 10$ and at relatively high $k$, whereas Figure 3(b) shows that $\mathcal{Q}$ peaks further out ($y^+ \approx 20$) and extends to the highest resolved $k$. Because $\mathcal{Q}$ is a difference of two large, correlated quadratic forms, strong cancellations occur when mapped to the wall.

### 3.1. *Variance attribution*

Figure 3(c,d) highlights how the source terms are mapped to the wall-pressure fluctuations by showing the instantaneous wall-pressure attribution maps for $\mathcal{L}$ and $\mathcal{Q}$. The attribution is defined as the fraction of the wall pressure at $k$ contributed by sources at height $y$. We define the attribution function $f_y(k)$ as

$$f_y(k) = \frac{\Re\{G(k,y)\,\widehat{\mathcal{M}}(y,k)\,\widehat{p}^{*}(k)\}}{|\widehat{p}(k)|^2}\ . \tag{3.1}$$

For each $k$, $\sum_y f_y(k) = 1$; positive values indicate in-phase contributions to the wall pressure and negative values indicate cancellation. The maps show that wavenumber contributions to $\mathcal{L}$ (Figure 3(c)) are always positive and distributed over a range of wall-normal heights at $k \lesssim 10$ and become more concentrated over a single height as $k$ increases. The contributions to $p$ from $\mathcal{Q}$ (Figure 3(d)) are similar to $\mathcal{L}$ for $k \gtrsim 10$. For $k \lesssim 10$, however, the contributions to $p$ become more localized with strong positive and

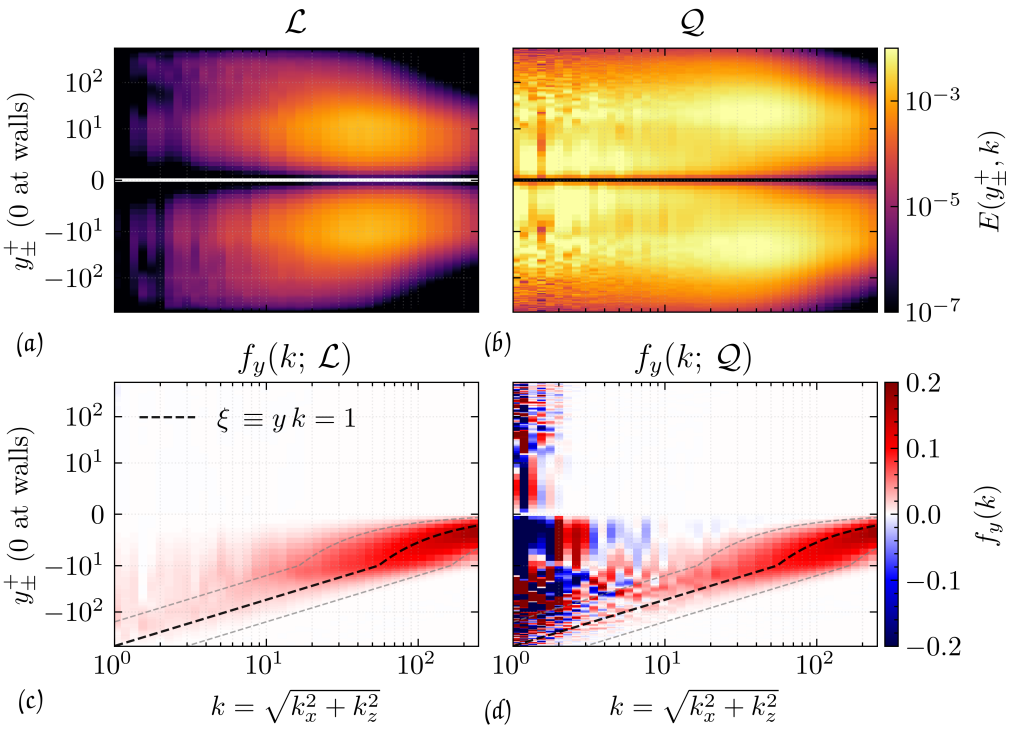


FIGURE 3. Ring-averaged $y^+$–$k$ spectra of (a) linear $\mathcal{L}$ and (b) nonlinear $\mathcal{Q}$ sources, as well as the corresponding wall-pressure attribution maps to the bottom wall for (c) linear pressure and (d) nonlinear pressure. (c,d) The black dashed line indicates $k\,y = 1$, and the two gray lines indicate $\xi = 0.3$ and $\xi = 3$. The kink in the lines is due to the change from log to linear scaling at $y^+ = 10$ toward the channel wall.

negative contributions to the integral making up $p(k)$, as well as significant contributions from structures from the other channel wall.

### 3.2. *Elliptical attenuation*

Heuristically, the elliptical attenuation reflects the balance between the algebraic spectral decay of the source and the exponential decay of the Green's kernel with wall-normal distance. For a wall-parallel wavenumber magnitude $k$ at height $y$, the wall-weighted amplitude scales as

$$|G(k,y)\,\widehat{\mathcal{M}}(y,k)| \;\sim\; \frac{e^{-ky}}{k} \times \big[\text{algebraic source decay in } k\big], \tag{3.2}$$

where the factor $e^{-ky}$ comes from the Green's kernel for $k \gg 1$ (Eq. (2.8)), so that contributions from a layer at $y$ are rapidly attenuated once $k\,y \gg 1$. Accordingly, we define the effective envelope of wall-source communication by a fixed iso-attenuation criterion on the kernel; for instance,

$$e^{-ky} = e^{-1} \quad \Longleftrightarrow \quad \xi \equiv k\,y = 1, \tag{3.3}$$

where $\xi = \mathcal{O}(1)$ denotes one $e$-fold of attenuation. For $\xi \ll 1$, the kernel hardly filters (and the communication is then controlled by the source spectrum), whereas for $\xi \gg 1$,

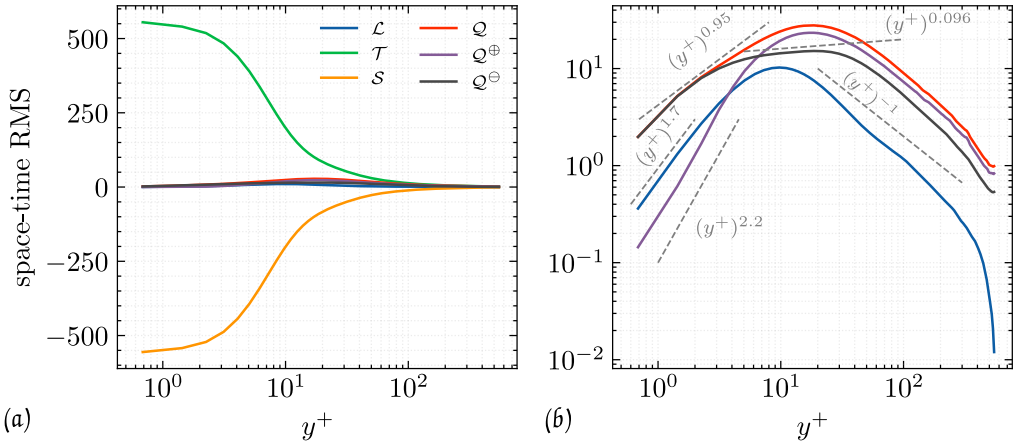


FIGURE 4. Profiles of the r.m.s. of the Poisson source components versus $y^+$. (a) The individual components, $\mathcal{L}$, $\mathcal{T}$, $-\mathcal{S}$, and $\mathcal{Q}$, and the sign-split parts, $\mathcal{Q}^\oplus$ and $\mathcal{Q}^\ominus$ (Eqs. (2.1),(2.2), and (3.4)). (b) Log–log view of selected curves.

the exponential damping dominates and suppresses the contribution. The line $\xi = 1$ therefore serves as a practical elliptical attenuation boundary in $(k, y)$-space.

Figure 3(c,d) plots the $\xi = 1$ line as an approximate envelope: High-$k$ contributions from a given layer lie predominantly on or slightly above this curve, while the low-$k$ contributions ($k \lesssim 10$) extend more broadly, with $\xi = 1$ providing an upper bound on their influence. (We reiterate that the bound on the $e^{-ky}$ decay in Eq. (2.8) is valid on $k \gg 1$.) Figure 3(c,d) also plots lines at $\xi = 0.3$ and $\xi = 3$ to give a sense of the $O(1)$ range of the elliptical attenuation.

### 3.3. *Enstrophy- or strain-driven* $\mathcal{Q}$

When $\mathcal{T} > \mathcal{S}$ (Eq. (2.2)), $\mathcal{Q}$ is enstrophy driven and that local region contributes positively to the integral making up the pressure (Eq. (2.2)). When $\mathcal{T} < \mathcal{S}$, $p$ is strain driven and the integral to the pressure has negative contributions.

To glean further insight into the statistically significant strain–enstrophy balance, we look at the r.m.s. of $\mathcal{Q}$. Additionally, we split $\mathcal{Q}$, so that

$$\mathcal{Q}^\oplus = |\max(\mathcal{Q}, 0)|, \qquad \mathcal{Q}^\ominus = |\min(\mathcal{Q}, 0)|, \tag{3.4}$$

and treat their r.m.s. profiles separately.

### 3.4. *Root mean square of the source components*

Profiles of the r.m.s. of the Poisson sources versus $y^+$ quantify the available amplitude before cancellation by sign and by kernel weighting. Figure 4(a) shows that $\mathcal{T}$ and $-\mathcal{S}$ balance strongly, with magnitudes dominating over the r.m.s. of the other components. Figure 4(b) shows the r.m.s. profiles with a logarithmic ordinate and $\mathcal{T}$ and $-\mathcal{S}$ removed. In line with the instantaneous picture in Figure 3(a,b), $\mathcal{L}$ peaks at $y^+ \approx 10$ and decays with $y^{+-1}$, whereas $\mathcal{Q}$ peaks at $y^+ \approx 20$ and remains significantly larger than $\mathcal{L}$ across most of the domain, decaying at the same rate further from the wall.

The $Q^\oplus/Q^\ominus$ split reveals enstrophy- versus strain-dominated contributions to $Q$, where the strain-dominated part ($Q^\ominus$) contributes negatively to the wall-pressure integral. We find that $Q^\ominus > Q^\oplus$ for $y^+ \lesssim 7$; for $y^+ \gtrsim 7$, $Q^\oplus$ becomes comparable to or exceeds $Q^\ominus$.

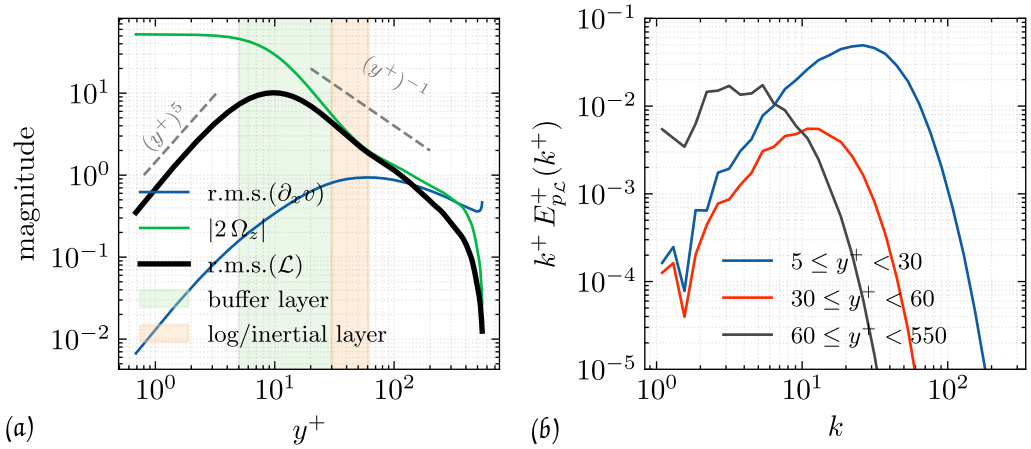


FIGURE 5. (a) Wall-normal trends at $\delta^+ \approx 550$: r.m.s.$(\partial_x v)$ (blue), $|2\Omega_z|$ (green), and r.m.s.$(\mathcal{L})$ (black). Shaded bands mark the buffer and logarithmic windows. (b) Premultiplied, inner-scaled wall-pressure spectrum carried by $\mathcal{L}$, shown as $k^+ E^+_{p_\mathcal{L}}(k^+)$, when the integral in Eq. (2.7) is restricted to three slabs on the lower half-channel: $5 \le y^+ < 30$ (blue), $30 \le y^+ < 2.6\sqrt{\delta^+}$ (orange; $\sim$60 at $\delta^+ \approx$550), and $2.6\sqrt{\delta^+} \le y^+ < \delta^+$ (gray).

In the viscous sublayer ($y^+ \lesssim 7$), $\mathcal{Q}^{\ominus}_{\rm rms} > \mathcal{Q}^{\oplus}_{\rm rms}$ (strain excess dominates). For $y^+ \gtrsim 7$, $\mathcal{Q}^{\oplus}$ becomes comparable to or exceeds $\mathcal{Q}^{\ominus}$ as intermittent enstrophy bursts appear in the buffer/log layers.

## 4. Near-wall behavior of the linear source

The universal inner function in the wall-pressure spectra made explicit by Massey *et al.* (2025) is defined only at sufficiently high $\delta^+$. In practice, the proposed $B_\mathcal{L}$ offset in Eq. (1.1) is an asymptotic limit on the integration of this inner function to $\langle p^{+2} \rangle$. The link between this inner function and the linear source $\mathcal{L}$ is made by considering the near-wall behavior of $\mathcal{L}$ and its mapping to the wall.

Figure 5(a) shows the r.m.s. of the factors that form the product $\mathcal{L} = 2\Omega_z\, \partial_x v$; in the viscous sublayer and lower buffer, r.m.s.$\,\mathcal{L}$ increases steeply [r.m.s.$\,\mathcal{L} \sim (y^+)^5$ for $1 \lesssim y^+ \lesssim$ 10–15], peaks near $y^+ \approx$ 20–30, and then decays approximately as $(y^+)^{-1}$ across the inertial layer. The behavior of $\mathcal{L}$ is shaped by the competing trends of its factors.

The mean spanwise-vorticity magnitude $|\Omega_z|$ is highest at the wall and stays around this value in the viscous sublayer, then rounds off and decays across the buffer and log layers, following the $1/(\kappa y^+)$ envelope in the inertial layer. The $\partial_x v$ trend is more complex. It is small at the wall and increases rapidly across the viscous sublayer, buffer, and inertial layers peaking in the buffer layer and slowly decaying in the wake region.

Two effects make the wall imprint of $\mathcal{L}$ essentially a near-wall contribution. The first is amplitude decay at wall-relevant scales. For a source layer at height $y$, the ring weighting from the Green's mapping and the derivative content of the source select wavenumbers with $\xi = O(1)$. Contributions with $\xi \gg 1$ are exponentially attenuated by the kernel, while those with $\xi \ll 1$ are reduced by the $k^{-1}$ (or steeper) decay of the source spectra

(see Section 2). In inner units, $\xi = O(1)$ implies $k^+ = \xi/y^+$, so for the selected modes

$$(\partial_x v)^+ \sim k^+ v^+ = \frac{\xi}{y^+}\, v^+ \ . \tag{4.1}$$

Since $v^+$ varies only weakly across the inertial layer, r.m.s.$(\partial_x v)^+ \sim c_v\, \xi/y^+$. With $|2\Omega_z|^+ = -\partial_{y^+} U^+ \sim 1/(\kappa y^+)$ across the log region, we obtain

$$\text{r.m.s.}\, \mathcal{L}^+(y) \ \sim \ \frac{c_v\, \xi}{\kappa (y^+)^2} \ . \tag{4.2}$$

That is, the wall-relevant portion of $\mathcal{L}$ decays in proportion to $(y^+)^{-2}$; for instance, Figure 5(a) shows a–steeper than the plotted–decay of $(y^+)^{-1}$ decay in the range $10 \lesssim y^+ \lesssim 30$. This sharper decay fixes the Reynolds number sensitivity: Contributions from increasingly remote inertial layer heights fall off to less than $1/\delta^+$ by the start of the inertial layer, although modulation effects persist in the low-wavenumber contributions.

The second effect is elliptic attenuation. The wall kernel damps sources with increasing $\xi$ (see Section 3.2). Figure 5(b) plots the premultiplied inner-unit spectrum $k^+ E^+_{p_\mathcal{L}}(k^+)$ for three wall-normal slabs. In this representation, the area under each curve equals that slab's contribution to $\langle p^{+2}_\mathcal{L} \rangle$. The near-wall band ($5 \le y^+ < 30$) dominates across the energy-containing $k^+$, while the log layer band is weaker by a decade around the spectral peak and by more than 3 decades at large $k^+$. The residual outer/wake band contributes only at the very lowest $k^+$ and is significant in the $k \lesssim 10$ region. This is consistent with the relaxation of the elliptical attenuation noted in Section 3, while the cumulative contribution to $\langle p^{+2}_\mathcal{L} \rangle$ is negligible due to the rapid decay of $k^+ \gtrsim 10$.

Combining these two effects reveals that the per-decade contribution of $\mathcal{L}$ to $\langle p^{+2} \rangle$ scales as

$$|G|^2 \Big[\text{r.m.s.}\, \mathcal{L}^+\Big]^2 \times (2\pi k\, \mathrm{d}k) \ \propto \ y^{+2} \times y^{+-4}\, \mathrm{d}\ln y \ = \ y^{+-2}\, \mathrm{d}\ln y, \tag{4.3}$$

so integrating from the buffer layer edge to $O(\delta^+)$ yields an $O(1)$ number set by the inner limit, namely a Reynolds-independent offset. Henceforth, we treat $p^+_\mathcal{L}$ as an $O(1)$ buffer layer contribution; the $\delta^+$ trend in $\langle p^{+2} \rangle$ must arise from $\mathcal{Q}$. We denote this offset as $B_\mathcal{L}$ and do not expect it to vary appreciably with $\delta^+$.

## 5. Fissures as compact carriers of the source terms

The mechanistic link between the pressure-Poisson sources and the vortical-fissure picture of the inertial layer rests on the compact spatial support of the sources within the fissures. We define compact support as regions where the source terms are significantly nonzero and spatially confined. Figure 6 summarizes the formation and alignment of these fissures and their variation with $\delta^+$. We consider a single fissure neighborhood and introduce local coordinates

$$(s, n, t) = (x, y, z) + O(\theta), \qquad \theta \ll 1, \tag{5.1}$$

with $s$ (approximately streamwise), $n$ (approximately wall-normal), and $t$ (approximately spanwise). In the fissure frame, the velocity is decomposed into a fissure-aligned (skeletal)

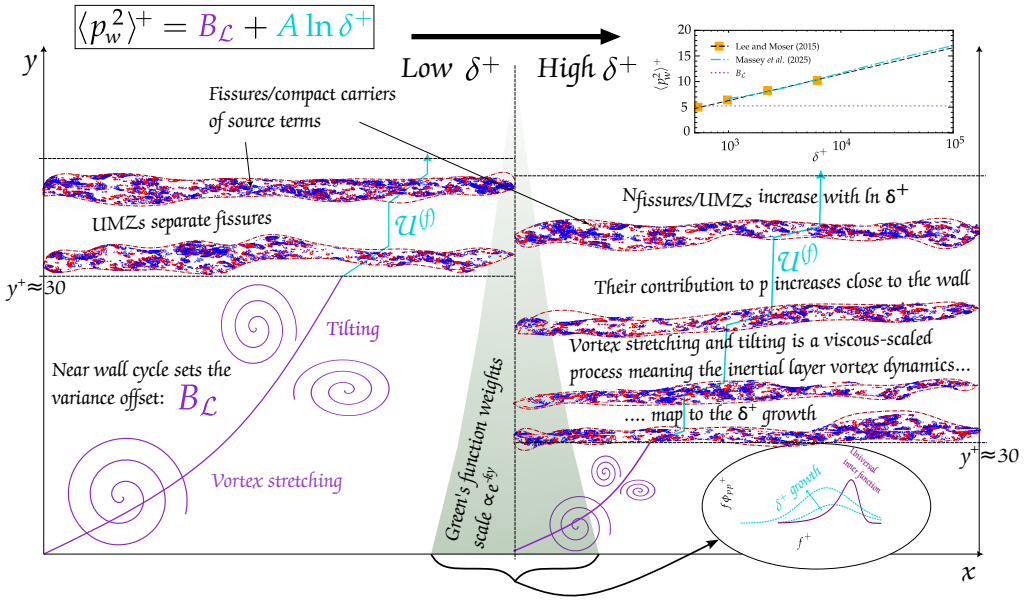


FIGURE 6. Schematic of the physical process that yields the $\ln\delta^+$ growth of $\langle p^{+2}\rangle$. Vortex stretching/tilting produces thin, sheetlike fissures that carry the Poisson sources compactly across the inertial layer and imprint at the wall through an elliptic Green's mapping that favors low wall-parallel wavenumbers.

mean (Bautista *et al.* 2019) and residuals,

$$\tilde{u}^{(f)}(s,n,t) \;=\; \mathcal{U}^{(f)}(n) \;+\; u^{(f)}(s,n,t) \;\approx\; \mathcal{U}^{(f)}(y) \;+\; u^{(f)}(x,y,z), \tag{5.2a}$$

$$\tilde{v}^{(f)}(s,n,t) \;=\; v^{(f)}(s,n,t) \;\approx\; v^{(f)}(x,y,z), \tag{5.2b}$$

$$\tilde{w}^{(f)}(s,n,t) \;=\; w^{(f)}(s,n,t) \;\approx\; w^{(f)}(x,y,z), \tag{5.2c}$$

where $\mathcal{U}^{(f)}$ is the fissure-aligned most probable (UMZ-like) streamwise profile and $u^{(f)}$, $v^{(f)}$, and $w^{(f)}$ are zero mean under a fissure-aligned conditional average, $\langle (u_i)^{(f)}\rangle_f = 0$. The global mean remains $U_i = (U(y),0,0)$. Consistent with the UMZ-vortical-fissure picture, the skeletal profile is a near step with jump $\Delta\mathcal{U}^{(f)} = O(u_\tau)$ across thickness $\delta^{(f)}$, such that

$$\partial_y \mathcal{U}^{(f)} \;\sim\; \frac{\Delta\mathcal{U}^{(f)}}{\delta^{(f)}} \;\approx\; \frac{u_\tau}{\delta^{(f)}} \quad \text{with} \quad \delta^{(f)} \ll \ell_{s,t}. \tag{5.3}$$

This yields the local velocity gradient

$$\partial_i \tilde{u}_j^{(f)} \;\approx\; \underbrace{\begin{pmatrix} 0 & 0 & 0 \\ \partial_y \mathcal{U}^{(f)} & 0 & 0 \\ 0 & 0 & 0 \end{pmatrix}}_{\text{mean fissure shear}} + \partial_i u_j^{(f)}\,. \tag{5.4}$$

To expose compact support of the nonlinear source $\mathcal{Q} = -\partial_i\partial_j(u_i u_j)$ in local coordinates, we write the fluctuations as the sum of a skeletal contribution (support confined

to the fissure) and residuals that are zero mean in the fissure frame,

$$u_i \;\approx\; \underbrace{\big(\mathcal{U}^{(f)} - U\big)}_{U^{(sk)}(y)} \;+\; \underbrace{\big(u^{(f)}, v^{(f)}, w^{(f)}\big)}_{u^\star(s,n,t)}. \tag{5.5}$$

Substituting Eq. (5.5) yields

$$\mathcal{Q} \;=\; -\partial_i\partial_j(U_i^{(sk)}U_j^{(sk)}) \;-\; 2\,\partial_i\partial_j\big(U_i^{(sk)}u_j^\star\big) \;-\; \partial_i\partial_j\big(u_i^\star u_j^\star\big). \tag{5.6}$$

Because $U^{(sk)}$ has only an $s$ component depending on $n$, $\partial_i\partial_j(U_i^{(sk)}U_j^{(sk)}) = 0$. The last term is broadband and volumetric in the UMZ interior; under the elliptic Green's mapping, it is less efficiently transmitted to the wall than fissure-aligned, low-$k$ contributions (see below). The cross-term simplifies to

$$-\,2\,\partial_x\partial_y\big(U^{(sk)}v^{(f)}\big) = -\,2\,\partial_x\Big[\big(\partial_y U^{(sk)}\big)\,v^{(f)} + U^{(sk)}\,\partial_y v^{(f)}\Big]. \tag{5.7}$$

In the fissure neighborhood, $\delta^{(f)} \ll \ell_{s,t}$, so $\partial_n \gg \partial_{s,t}$ and the first product, proportional to $\partial_y U^{(sk)} \sim u_\tau/\delta^{(f)}$, dominates. Thus,

$$\mathcal{Q}^{(f)} \;\approx\; -\,2\,\partial_x\partial_y\Big(U^{(sk)}\,v^{(f)}\Big) \tag{5.8}$$

is compactly supported on the fissure. Integrating across the $O(\delta^{(f)})$ thickness yields the fissure-source density

$$\int \mathcal{Q}^{(f)}\,dy \;\approx\; -\,2\,\partial_x\,[\![U^{(sk)}\,v^{(f)}]\!], \qquad [\![\cdot]\!] := \text{jump across the fissure.} \tag{5.9}$$

The spectral content of $\mathcal{Q}^{(f)}$ is governed by along-fissure gradients of the flux $U^{(sk)}v^{(f)}$. Since the along-fissure length scales satisfy $\ell_{s,t} \gg \delta^{(f)}$, the resulting content is biased to low wall-parallel wavenumbers.

For the linear source, $\partial_n U_s \neq 0$ only within the fissure. Thus,

$$\mathcal{L}^{(f)} \;=\; -\,2\,(\partial_n U)\,\partial_s v^{(f)} \;\approx\; -\,2\,(\partial_y U)\,\partial_x v^{(f)} \tag{5.10}$$

is likewise localized by $\partial_n U$, with its spectrum set by the along-fissure gradients $\partial_s v^{(f)}$ (low $k$). In short, both $\mathcal{Q}^{(f)}$ and $\mathcal{L}^{(f)}$ are fissure supported and streamwise biased in wavenumber.

Finally, the wall imprint of these compact sources is dictated by the elliptic Green's function. Because the wall-parallel Green's weight decays approximately as $e^{-k\,y}$, low wall-parallel wavenumbers suffer weak attenuation, while high-$k$ content from the UMZ interior is strongly filtered. Consequently, fissure-aligned sources with low along-fissure $k$ transmit efficiently to the wall compared with broadband interior fluctuations. This picture is consistent with the UMZ-vortical-fissure structure in which $\Delta U = O(u_\tau)$ across fissures of thickness $\delta^{(f)} \sim \delta/\sqrt{\delta^+}$ (Klewicki 2013; Bautista *et al.* 2019).

## 6. Discussion and consequences

These results link the source terms of the pressure Poisson equations to physical processes that enable us to clarify the $\delta^+$ scaling of $\langle p^{+2}\rangle$. We start by introducing the variance attribution map that elucidates the $\xi = O(1)$ attenuation of structures for $k \lesssim 10$. We then look at the energetic structure of the sources, showing that $\mathcal{L}$ is concentrated in the buffer layer, while $\mathcal{Q}$ is most energetic in the inertial layer. $\mathcal{Q} = \mathcal{T} - \mathcal{S}$ (Eq. (2.2)) is

the difference of two large, strongly correlated quadratic forms; their partial cancellation is central to how $\mathcal{Q}$ maps to the wall. Next, we show that $\mathcal{L}$ is linked to the near-wall process that subsequently provides an $O(1)$ offset to the observed $\langle p^{+2}\rangle(\delta^+)$ growth. Finally, we show that fissures separating UMZs in the inertial layer act as compact carriers of these source terms.

The conceptual link between the source terms and processes in the turbulent boundary layer allows us to infer scalings for the sources and, via consideration of the Green's function weighting, $\langle p^{+2}\rangle(\delta^+)$. The fissure thickness, when scaled by outer length, decreases approximately as $1/\sqrt{\delta^+}$ while the streamwise velocity jump across a fissure is $O(u_\tau)$. Furthermore, the number of fissures increases approximately as $\ln\delta^+$ (Bautista *et al.* 2019), and the fraction of total vorticity contained in the fissures increases with $\delta^+$ (Klewicki 2013). The fissure thickness sets the scale for the normal gradients in Eqs. (5.8)-(5.10), while the velocity jump sets the scale for $U^{(sk)}$. The increasing number of fissures and their increasing proportion of total vorticity content with $\delta^+$ imply that the amplitude and intermittency of $\mathcal{Q}$ increase with $\delta^+$, while $\mathcal{L}$ remains approximately constant as it is tied to near-wall processes. Therefore, considering the observed form of the wall-pressure-variance scaling,

$$\langle p^{+2}\rangle \;=\; B_{\mathcal{L}} + A_{\mathcal{Q}}\ln\delta^+ \;,$$

we identify $B_{\mathcal{L}}$ as the $\delta^+$-independent offset from $\mathcal{L}$ and $A_{\mathcal{Q}}\ln\delta^+$ as the $\delta^+$-dependent contribution from $\mathcal{Q}$. $A_{\mathcal{Q}}$ is therefore tied to the fissure statistics and their evolution with $\delta^+$, and future work will seek to quantify this connection.

This picture of the mechanisms driving the source terms supports the bimodal nature of the premultiplied wall-pressure spectrum identified by Massey *et al.* (2025). The universal inner function (their $g_1$) arises from the near-wall contribution of $\mathcal{L}$, and the break frequency is defined as the frequency/length scale where the buffer layer contribution is at its maximum. The outer function (their $g_2$) arises from the inertial layer contribution of $\mathcal{Q}$, with the break frequency associated with length scales on the scale of the boundary layer thickness (consistent with inertial layer structures). The present framework therefore provides a mechanistic underpinning for the spectral decomposition of Massey *et al.* (2025).

For control and design, where to act follows from the source split. Targeting the inertial layer to weaken intensity or intermittency reduces $A_{\mathcal{Q}}$, while targeting the buffer layer primarily modifies $\mathcal{L}$ and therefore the offset $B_{\mathcal{L}}$. Because $\xi = O(1)$, actuation localized at $y_a$ imprints most strongly near $k \sim O(1)/y_a$, offering a direct spectral target for feedback or open-loop strategies aimed at the most relevant per-decade inertial layer contribution.

In summary, this conceptual picture maps the interface between UMZs in turbulent boundary layers to the spectral content of wall pressure and provides a compact lever for models, diagnostics, and control. By tracing how sheetlike structures feed the nonlinear Poisson source and are transmitted to the wall through a radially weighted Green's mapping, this framework connects wall-pressure behavior to a vorticity-centric description of inertial layer dynamics (Klewicki 2013) and supplies a mechanistic rationale for the logarithmic growth highlighted by matched-asymptotic theory (Panton *et al.* 2017).

*Acknowledgements*

The support of ONR grant # N000142312833 is gratefully acknowledged as well as support from DARPA under award # HR0011-24-9-0465.

## REFERENCES


Anantharamu, S. & Mahesh, K. 2020 Analysis of wall-pressure fluctuation sources from direct numerical simulation of turbulent channel flow. *J. Fluid Mech.* **898**, A17.

Bautista, J. C. C., Ebadi, A., White, C. M., Chini, G. P. & Klewicki, J. C. 2019 A uniform momentum zone–vortical fissure model of the turbulent boundary layer. *J. Fluid Mech.* **858**, 609–633.

Bradshaw, P. 1967 'Inactive' motion and pressure fluctuations in turbulent boundary layers. *J. Fluid Mech.* **30**, 241–258.

Bradshaw, P. & Koh, Y. 1981 A note on Poisson's equation for pressure in a turbulent flow. *Phys. Fluids* **24** (4), 777.

Chang, P. A., Piomelli, U. & Blake, W. K. 1999 Relationship between wall pressure and velocity-field sources. *Phys. Fluids* **11**, 3434–3448.

Chauhan, K., Philip, J., De Silva, C. M., Hutchins, N. & Marusic, I. 2014 The turbulent/non-turbulent interface and entrainment in a boundary layer. *J. Fluid Mech.* **742**, 119–151.

Choi, H. & Moin, P. 1990 On the space-time characteristics of wall-pressure fluctuations. *Phys. Fluids A* **2**, 1450–1460.

Dacome, G., Lazzarini, L., Talamelli, A., Bellani, G. & Baars, W. J. 2025 Scaling of wall-pressure–velocity correlations in high-Reynolds-number turbulent pipe flow. *J. Fluid Mech.* **1013**, A48.

De Silva, C. M., Philip, J., Hutchins, N. & Marusic, I. 2017 Interfaces of uniform momentum zones in turbulent boundary layers. *J. Fluid Mech.* **820**, 451–478.

Deshpande, R., Hassanein, A. & Baars, W. J. 2025*a* Source locations and convection velocities of outer-scaled wall-pressure fluctuations in canonical turbulent boundary layers. arXiv:2508.19940 [physics].

Deshpande, R., Vinuesa, R., Klewicki, J. & Marusic, I. 2025*b* Active and inactive contributions to the wall pressure and wall-shear stress in turbulent boundary layers. *J. Fluid Mech.* **1003**, A24.

Farabee, T. M. & Casarella, M. J. 1991 Spectral features of wall pressure fluctuations beneath turbulent boundary layers. *Phys. Fluids A* **3**, 2410–2420.

Flores, O. & Jiménez, J. 2006 Effect of wall-boundary disturbances on turbulent channel flows. *J. Fluid Mech.* **566**, 357–376.

Fritsch, D., Vishwanathan, V., Duetsch-Patel, J., Gargiulo, A., Lowe, K. T. & Devenport, W. J. 2020 The pressure signature of high Reynolds number smooth wall turbulent boundary layers in pressure gradient family. *AIAA Paper* 2020-3066.

Fritsch, D. J., Vishwanathan, V., Todd Lowe, K. & Devenport, W. J. 2022 Fluctuating pressure beneath smooth wall boundary layers in nonequilibrium pressure gradients. *AIAA J.* **60**, 4725–4743.

Gerolymos, G. A., Sénéchal, D. & Vallet, I. 2013 Wall effects on pressure fluctuations in turbulent channel flow. *J. Fluid Mech.* **720**, 15–65.

Gibeau, B. & Ghaemi, S. 2021 Low- and mid-frequency wall-pressure sources in a turbulent boundary layer. *J. Fluid Mech.* **918**, A18.

Heisel, M., De Silva, C. M., Katul, G. G. & Chamecki, M. 2022 Self-similar geometries within the inertial subrange of scales in boundary layer turbulence. *J. Fluid Mech.* **942**, A33.

Hoyas, S. & Jiménez, J. 2006 Scaling of the velocity fluctuations in turbulent channels up to $Re_\tau = 2003$. *Phys. Fluids* **18**, 011702.

Hu, Z. W., Morfey, C. L. & Sandham, N. D. 2006 Wall pressure and shear stress spectra from direct simulations of channel flow. *AIAA J.* **44**, 1541–1549.

Huang, Y., Toedtli, S. S., Chini, G. P. & McKeon, B. J. 2025 Spatio-temporal characterization of nonlinear forcing and response in turbulent channel flow. arXiv:2503.06915 [physics].

Kim, J. 1989 On the structure of pressure fluctuations in simulated turbulent channel flow. *J. Fluid Mech.* **205**, 421.

Klewicki, J. C. 2013 A description of turbulent wall-flow vorticity consistent with mean dynamics. *J. Fluid Mech.* **737**, 176–204.

Klewicki, J. C., Priyadarshana, P. J. A. & Metzger, M. M. 2008 Statistical structure of the fluctuating wall pressure and its in-plane gradients at high Reynolds number. *J. Fluid Mech.* **609**, 195–220.

Lee, M. & Moser, R. D. 2015 Direct numerical simulation of turbulent channel flow up to. *J. Fluid Mech.* **774**, 395–415.

Mansour, N. N., Kim, J. & Moin, P. 1988 Reynolds-stress and dissipation-rate budgets in a turbulent channel flow. *J. Fluid Mech.* **194**, 15–44.

Massey, J. M. O., Smits, A. J. & McKeon, B. J. 2025 Eddy population based model for the wall-pressure spectrum at high Reynolds number. arXiv:2507.23098 [physics].

Meinhart, C. D. & Adrian, R. J. 1995 On the existence of uniform momentum zones in a turbulent boundary layer. *Phys. Fluids* **7**, 694–696.

Morrill-Winter, C. & Klewicki, J. 2013 Influences of boundary layer scale separation on the vorticity transport contribution to turbulent inertia. *Phys. Fluids* **25**, 015108.

Panton, R. L., Lee, M. & Moser, R. D. 2017 Correlation of pressure fluctuations in turbulent wall layers. *Phys. Rev. Fluids* **2**, 094604.

Pirozzoli, S. & Wei, T. 2025 On pressure fluctuations in the near-wall region of turbulent flows. *J. Fluid Mech.* **1010**, A10.

Schlatter, P. & Örlü, R. 2010 Assessment of direct numerical simulation data of turbulent boundary layers. *J. Fluid Mech.* **659**, 116–126.

Toedtli, S., L. A. . M. B. J. 2025 Coupled dynamics of wall pressure and transpiration, with implications for drag reduction. *J. Fluid Mech.* **1019**, A18.

Yang, B. & Yang, Z. 2022 On the wavenumber–frequency spectrum of the wall pressure fluctuations in turbulent channel flow. *J. Fluid Mech.* **937**, A39.